OPTICAL REVIEW Vol. 21, No. 5 (2014) 479–485

Coherence Three-Dimensional Imaging Spectrometry Based on Measurement of Rotated-Hyperbolic Volume Interferograms

Masaki OBARA* and Kyu YOSHIMORI

Department of Electrical Engineering and Computer Science, Graduate School of Engineering, Iwate University, Morioka 020-8551, Japan

(Received May 1, 2014; Accepted July 18, 2014)

A new interferometric technique to obtain three-dimensional multispectral images of spatially incoherent polychromatic-source distributions is investigated. This technique is based on the measurement of a new type of volume interferogram, herein called the rotated-hyperbolic volume interferogram, which can be obtained by existing interferometer together with a novel aperture synthesis. This paper reports the first demonstration of the method: measurement of a monochromatic point source. The results obtained from this measurement included three-dimensional spatial information and spectral information corresponding to the impulse response function defined over a four-dimensional space. These experimental results confirmed that the imaging characteristics, particularly depth resolution, of the new method are superior to those of previous methods.

Keywords: coherence imaging, three-dimensional imaging, interferometry, digital holography, spectrometry

1. Introduction

Michelson invented the stellar interferometer, now known as the Michelson stellar interferometer (MSI), in which the measured angular diameter of a star can be determined from contrast of the lateral interference fringes of propagating light.[1)] The later-developed incoherent holography works by the same principle. Now, MSIs are often used to measure the three-dimensional (3-D) profile of an object illuminated by a spatially incoherent monochromatic source. Michelson also suggested that measuring the interference pattern created by superposition of two wavefronts propagating through different optical distances from a common light source would yield the continuous spectrum of that light source. This insight is the basis of Fourier transform spectroscopy.

Interferometric multi-spectral imaging[2)] is a technique that obtains a set of spectral components of two-dimensional (2-D) images by combining the principles of the above two interferometric methods. Yoshimori extended this technique to obtain a set of spectral components of 3-D images.[3)] An MSI measures the spatial correlation function across a lateral baseline. According to the Van Cittert–Zernike (VCZ) theorem, this spatial correlation function is proportional to the Fourier transform of the intensity distribution of the light source. By generalizing the VCZ theorem to describe the correlation between the optical fields at two distinct 3-D points, it is possible to obtain the 3-D information of a monochromatic object.[4)] Other recently proposed techniques for interferometric 3-D imaging include recording incoherent holograms by Sagnac radial shearing interferometry[5)] and comparing the different curvatures of two wavefronts propagating from a polychromatic object.[6)] Thus, in the branch of optics concerned with incoherent holography, we may find a variety of ideas; these include techniques to obtain 3-D monochromatic images, RGB color images, and spectral components of 2-D images.[7–9)] Additionally, Marks et al. report that it is possible to obtain fully 3-D images of spatially incoherent objects by combining cone beam tomography and interferometric measurement from a rotational shear interferometer.[10)]

Interferometric methods to obtain both the 3-D spatial information and the spectral information of a usual polychromatic object simultaneously without using coherent illumination, dispersion elements, or image-forming optical elements (such as lenses) have been previously investigated.[11–13)] These proposed methods use interferometric techniques and signal processing only. These methods use a two-wavefront folding interferometer and synthetic aperture technique. Two different signal-processing algorithms were proposed; both which are based on measurement of a five-dimensional (5-D) spatial correlation function. The two methods differ in the selection rule by which each method performs synthetic aperture processing. The first of these rules produces a spherical-type (S-type) volume interferogram.[11,12)] Experimental results were given for retrieving the 3-D position and spectrum of a monochromatic point source and for planar light sources of different continuous spectra located at different positions. The other selection rule produces a hyperbolic-type (H-type) volume interferogram.[13)] The recorded fringe patterns of the volume interferogram obtained by the H-type method do not correspond directly to the phase distributions of the wavefront of many spectral components propagated from the measured object. However, further analysis shows that the H-type method gives 3-D imaging properties equivalent to those from S-type volume interferograms.

This paper presents a novel method of coherence 3-D imaging spectrometry. The method is based on the measurement of a new type of volume interferogram, herein called rotated-hyperbolic (RH) volume interferograms, obtained by an interferometer used in the previous method but with a different signal-processing procedure used for synthetic

*E-mail address: masaki@ql.cis.iwate-u.ac.jp

aperture processing. The fringe pattern of the volume interferogram obtained by the present method is hyperbolic. Although it looks like an H-type volume interferogram, the asymptotic surfaces of the hyperbolic fringe patterns are rotated by 45°. We will show that this volume interferogram offers improved 3-D imaging properties, particularly depth resolution.

In Sect. 2, we begin by summarizing the principle of the new method and showing its connection to the experimental system. In Sect. 3, we present experimental results. These results show notable properties of the present method concerning the lateral and depth resolutions; these properties will be summarized in Sect. 4.

2. Principle of the Method

2.1 *Measurement of 5-D interferogram*

In this section, we will describe the fundamental idea of the present method in conjunction with the experimental system used to test it. Figure 1 shows a schematic of the two-wavefront folding interferometer that was used in our experimental system. This type of interferometer measures the 5-D spatial correlation function. The measured object is set on the x–y stage. The wavefront propagated from the object is split by a beam splitter (BS). Each split wavefront is reflected by either the right-angle-prism P or the right-angle-prism P′. Because the apexes of the two prisms are orthogonal to each other, each split wavefront is reversed, from up to down or right to left, by P or P′. Those wavefronts are superposed again on the BS. The generated fringe pattern, called the *elementally interference pattern*, is detected by the 2-D array detector (CCD). In addition, the lens (L in the figure) projects the surface of the CCD onto a plane that contains the apex of the prism P′. This plane is regarded as the observation plane. Thus, the z-distance is measured from this observation plane. To introduce an optical path difference between the two wavefronts, one of the prisms may be displaced along the z-axis by the Piezo Translator (PZT). During interferometric measurement, the x–y stage and the PZT are moved stepwise and 2-D elementally interference patterns are recorded at each stage position. In Fig. 1, $\hat{x}$ and $\hat{y}$ stand for the x and y positions, respectively, of the apex of prism P′ or P, each of which is being adjusted by movement of the x–y stage, and Z denotes the optical path difference introduced by the PZT.

Therefore, the 2-D elementally interference patterns obtained by the CCD are arranged three-dimensionally in $(\hat{x}, \hat{y}, Z)$ space. Then, the whole data set may be regarded as 5-D interferogram. This 5-D interferogram is expressed as

$$I(x,y,\hat{x},\hat{y},Z) = \frac{1}{4}[\Gamma(\boldsymbol{r},\boldsymbol{r}) + \Gamma(\boldsymbol{r}',\boldsymbol{r}') + \Gamma(\boldsymbol{r}',\boldsymbol{r}) + \Gamma^*(\boldsymbol{r}',\boldsymbol{r})], \tag{1}$$

where $\Gamma(\boldsymbol{r}',\boldsymbol{r}) = \langle V^*(\boldsymbol{r}',t)V(\boldsymbol{r},t)\rangle$ denotes the spatial correlation function of the optical field $V(\boldsymbol{r},t)$ at points $\boldsymbol{r}$ and $\boldsymbol{r}'$, the angle bracket stands for the ensemble average, and the asterisk denotes complex conjugate. We suppress the time t in Γ because the optical field is assumed to be stationary in time. In Eq. (1), $\Gamma(\boldsymbol{r},\boldsymbol{r}) = \langle|V(\boldsymbol{r},t)|^2\rangle$ and $\Gamma(\boldsymbol{r}',\boldsymbol{r}') = \langle|V(\boldsymbol{r}',t)|^2\rangle$ are the optical intensities at points $\boldsymbol{r}$ and $\boldsymbol{r}'$, respectively. The position vectors $\boldsymbol{r}$ and $\boldsymbol{r}'$ in Eq. (1) are the superposed points of the optical fields reflected by prisms P and P′, respectively. These points are written as

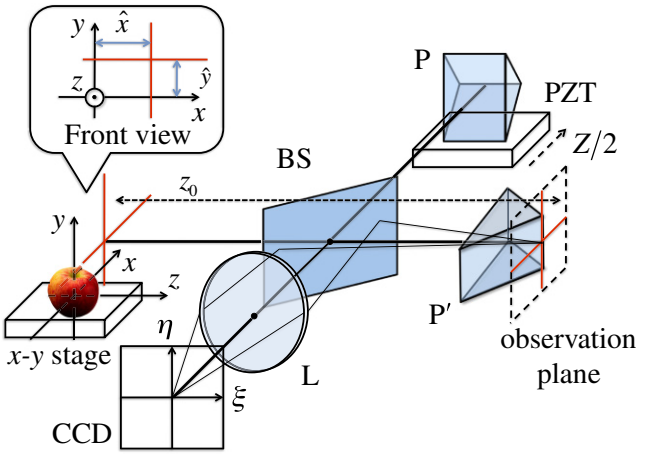

Fig. 1. (Color online) Schematic of two-wavefront folding interferometer.

$$\boldsymbol{r} = (x, 2\hat{y} - y, z_0 + Z), \tag{2a}$$

$$\boldsymbol{r}' = (2\hat{x} - x, y, z_0), \tag{2b}$$

where z_0 denotes the optical length between the observation plane and the origin of the Cartesian coordinate system fixed on the x–y stage. We note that the (x,y) origin of the Cartesian coordinate system and the origin of the coordinate system (ξ,η) taken over the observation plane do not always coincide because of the motion of the x–y stage. The relationship between the (x,y) coordinates and the (ξ,η) coordinates can be expressed as

$$x = \xi + \hat{x}, \tag{3a}$$

$$y = \eta + \hat{y}. \tag{3b}$$

On substituting Eq. (3) into Eq. (2), we may rewrite the 5-D interferogram in Eq. (1) in terms of (ξ,η) coordinates, which gives the form

$$I(\xi,\eta,\hat{x},\hat{y},Z) = \frac{1}{4}[\Gamma(\boldsymbol{r},\boldsymbol{r}) + \Gamma(\boldsymbol{r}',\boldsymbol{r}') + \Gamma(\boldsymbol{r}',\boldsymbol{r}) + \Gamma^*(\boldsymbol{r}',\boldsymbol{r})], \tag{4}$$

where the position vectors $\boldsymbol{r}$ and $\boldsymbol{r}'$ are expressed as

$$\boldsymbol{r} = (\xi + \hat{x}, -\eta + \hat{y}, z_0 + Z), \tag{5a}$$

$$\boldsymbol{r}' = (-\xi + \hat{x}, \eta + \hat{y}, z_0). \tag{5b}$$

2.2 *Recovery of a set of cross-spectral densities*

Next, because the optical field is stationary in time, the spatial correlation function $\Gamma(\boldsymbol{r}',\boldsymbol{r})$ recorded in the 5-D interferogram may be expressed as a superposition of the cross-spectral density $W_\omega(\boldsymbol{r}',\boldsymbol{r})$ for angular frequency $\omega = ck$

$$\Gamma(\boldsymbol{r}',\boldsymbol{r}) = \int_0^\infty W_\omega(\boldsymbol{r}',\boldsymbol{r})\, d\omega, \tag{6}$$

where c is the speed of light in free space and $k = 2\pi/\lambda$ is the wavenumber with wavelength λ. Thus, for a stationary

optical field, spectral components of the optical fields of different frequencies are mutually uncorrelated. We now define $\boldsymbol{r}'' = (\xi + \hat{x}, -\eta + \hat{y}, z_0)$, the shifted position of $\boldsymbol{r}$ onto the observation plane $z = z_0$, by setting $Z = 0$ in Eq. (5a). Within the paraxial regime and under the assumption that $z_0 \gg Z$, the cross-spectral density $W_\omega(\boldsymbol{r}', \boldsymbol{r}'')$ on the observation plane is related to $W_\omega(\boldsymbol{r}', \boldsymbol{r})$, which appears in the right-hand side of Eq. (6), by

$$W_\omega(\boldsymbol{r}', \boldsymbol{r}) = \exp(ikZ) W_\omega(\boldsymbol{r}', \boldsymbol{r}''). \tag{7}$$

On substituting Eq. (7) into Eq. (6), we obtain the following relationship between the measured spatial correlation function $\Gamma(\boldsymbol{r}', \boldsymbol{r})$ and the cross-spectral density $W_\omega(\boldsymbol{r}', \boldsymbol{r}'')$ defined over the observation plane:

$$\Gamma(\boldsymbol{r}', \boldsymbol{r}) = c \int_0^\infty W_\omega(\boldsymbol{r}', \boldsymbol{r}'') \exp(ikZ)\, dk. \tag{8}$$

Then, Eq. (8) can be inverted, expressing the cross-spectral density as the Fourier transform of the 5-D spatial correlation function

$$W_\omega(\boldsymbol{r}', \boldsymbol{r}'') = \frac{1}{2\pi c} \int \Gamma(\boldsymbol{r}', \boldsymbol{r}'') \exp(-ikZ)\, dZ, \tag{9}$$

where the integrand is taken over the actual extension of the interferogram with respect to Z. We now derive the cross-spectral density expressed in the left-hand-side of Eq. (9). The cross-spectral density $W_\omega(\boldsymbol{r}', \boldsymbol{r}'')$ is defined as the cross-correlation of the monochromatic component of the optical field $U_\omega(\boldsymbol{r}')$ at two points, $\boldsymbol{r}'$ and $\boldsymbol{r}''$. In our case, it is written as

$$\begin{aligned} W_\omega(\boldsymbol{r}', \boldsymbol{r}'') &= \langle U_\omega^*(\boldsymbol{r}') U_\omega(\boldsymbol{r}'') \rangle \\ &= \int \frac{S_\omega(\boldsymbol{r}_s)}{r' r''} \exp[ik(r'' - r')]\, d^3 r_s, \end{aligned} \tag{10}$$

where $S_\omega(\boldsymbol{r}_s)$ denotes the spectral density of the measured 3-D object at $\boldsymbol{r}_s = (x_s, y_s, z_s)$, $r' = |\boldsymbol{r}' - \boldsymbol{r}_s|$ and $r'' = |\boldsymbol{r}'' - \boldsymbol{r}_s|$ are the respective distances between the point on the object $\boldsymbol{r}_s$ and the points $\boldsymbol{r}'$ and $\boldsymbol{r}''$. Under the paraxial approximation and the assumption $z_0 \gg Z$, the cross-spectral density $W_\omega(\boldsymbol{r}', \boldsymbol{r}'')$ in the second expression of Eq. (10) may be rewritten in the following form:

$$W_\omega(\boldsymbol{r}', \boldsymbol{r}'') = \int S_\omega(\boldsymbol{r}_s) \exp\left[ik \frac{2\xi(\hat{x} - x_s) - 2\eta(\hat{y} - y_s)}{z} \right] d^3 r_s, \tag{11}$$

where $z = z_0 - z_s$ is the optical depth of the object, as measured from the observation plane. For simplicity, the distances r' and r'' in the denominator in Eq. (10) have been absorbed into the spectral density $S_\omega(\boldsymbol{r}_s)$. Equation (11) is a generalization of the VCZ theorem to the correlation between two points lying in the paraxial zone, locating a spatially incoherent object in the Fresnel domain. The goal of our method is to retrieve the 3-D distribution of $S_\omega(\boldsymbol{r}_s)$ for each spectral component.

In the proposed method, the two-wave front folding interferometer and a CCD are used to implement the recording of the 2-D elementally interference pattern. As shown in Eq. (4), the interference pattern being captured, which is an intensity image, including two self-correlation terms and two cross-correlation terms. Those can be separated in the procedure of recovery of cross-spectral densities. This is because, as shown in the integral region in Eq. (8), the cross-correlation term of interest $\Gamma(\boldsymbol{r}', \boldsymbol{r})$ contains positive frequency spectral components only. Then, by taking Fourier transform of Eq. (4) with respect to Z, the contribution of the cross-correlation term $\Gamma(\boldsymbol{r}', \boldsymbol{r})$ appears in positive frequency region, whereas its complex conjugate $\Gamma^*(\boldsymbol{r}', \boldsymbol{r})$, which contains negative frequency components only, appears in negative frequency region. Since the self-correlation terms are slowly varying functions of $\boldsymbol{r}$ or $\boldsymbol{r}'$, contributions from these terms locates around zero frequency. Thus, one can take cross-spectral density in Eq. (9), that is complex number in general, separately from RH volume interferogram, while contributions from other three terms are eliminated.

2.3 *Procedure to generate the RH volume interferogram*

To generate the volume interferogram, we apply a synthetic aperture technique to the 5-D interferogram; this technique uses a new selection rule to effect data rearrangement. In comparison to the previous method[11–13] under the same conditions, this new volume interferogram is more suitable for retrieving the source information. The first step in generating an RH volume interferogram is to choose one pixel value from each elementally interference pattern according to the new selection rule:

$$\xi = \hat{y}, \tag{12a}$$

$$\eta = -\hat{x}. \tag{12b}$$

We then introduce the parameters

$$X = 2\hat{x}, \tag{13a}$$

$$Y = 2\hat{y}, \tag{13b}$$

to rearrange the selected data. The rearranged data set forms the volume interferogram. Figure 2 shows a typical RH volume interferogram, obtained by the present method. The spatial correlation function for this volume interferogram is expressed in a similar form to that in Eq. (8) as

$$\begin{aligned} &\Gamma(\boldsymbol{R}_0 + \Delta\boldsymbol{\rho}; \boldsymbol{R}_0 + \hat{\boldsymbol{\rho}}) \\ &\quad = c \int_0^\infty W_\omega(\boldsymbol{R}_0 + \Delta\boldsymbol{\rho}_\perp; \boldsymbol{R}_0 + \hat{\boldsymbol{\rho}}_\perp) \exp(ikZ)\, dk, \end{aligned} \tag{14}$$

where $\boldsymbol{R}_0 = (0, 0, z_0)$ denotes the center of the observation plane, and the two points $\hat{\boldsymbol{\rho}}$ and $\Delta\boldsymbol{\rho}$ are defined as the mean position and the half-length of the separation between $\boldsymbol{\rho}$ and $\boldsymbol{\rho}'$, respectively. Here, the two vectors $\boldsymbol{\rho}$ and $\boldsymbol{\rho}'$ are defined by

$$\boldsymbol{\rho} = (\boldsymbol{\rho}_\perp, Z) = (X, Y, Z), \tag{15a}$$

$$\boldsymbol{\rho}' = (\boldsymbol{\rho}'_\perp, Z) = (Y, X, Z). \tag{15b}$$

The vector $\boldsymbol{\rho}$ represents three-dimensional shear from $\boldsymbol{R}_0$, and $\boldsymbol{\rho}'$ is located at the geometric reflection of $\boldsymbol{\rho}$ across the line $X = Y$. The mean position and the half-length vector in Eq. (14) may be rewritten as

$$\hat{\boldsymbol{\rho}} = \frac{\boldsymbol{\rho} + \boldsymbol{\rho}'}{2} = \left(\frac{X + Y}{2}, \frac{X + Y}{2}, Z \right) = (\hat{\boldsymbol{\rho}}_\perp, Z), \tag{16a}$$

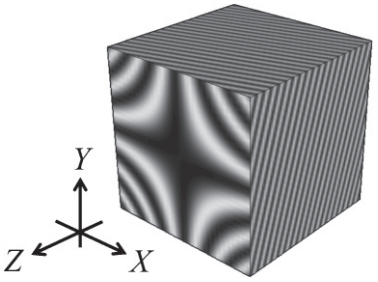

Fig. 2. Example of a theoretical RH volume interferogram for a monochromatic point source located at the origin of the Cartesian coordinate system.

$$\Delta\boldsymbol{\rho} = \frac{\boldsymbol{\rho} - \boldsymbol{\rho}'}{2} = \left(\frac{X-Y}{2}, \frac{Y-X}{2}, 0\right) = (\Delta\boldsymbol{\rho}_\perp, 0). \quad (16b)$$

Accordingly, the cross-spectral density in the second expression of in Eq. (10) is given by

$$\begin{aligned} &W_\omega(\boldsymbol{R}_0 + \Delta\boldsymbol{\rho}_\perp; \boldsymbol{R}_0 + \hat{\boldsymbol{\rho}}_\perp) \\ &= \int S_\omega(\boldsymbol{r}_s) \exp[i(\boldsymbol{k}_\perp \cdot \boldsymbol{\rho}'_\perp)] \exp\left(ik \frac{\hat{\boldsymbol{\rho}}_\perp^2 - \Delta\boldsymbol{\rho}_\perp^2}{2z}\right) d^3 r_s \\ &= \int S_\omega(\boldsymbol{r}_s) \exp[i(k_x Y + k_y X)] \exp\left(ik \frac{XY}{z}\right) d^3 r_s, \end{aligned} \quad (17)$$

where $\boldsymbol{k}_\perp = (k_x, k_y)$ is the lateral component of the wavenumber vector $\boldsymbol{k}$ directed from a point $\boldsymbol{r}_s$ on the object to the center of the observation plane, with $k_x = -kx_s/z$ and $k_y = -ky_s/z$. We see that the parameters X and Y in the linear phase factor appeared in the second expression of Eq. (17) in reversed positions. We also note that the quadratic phase factor depends on the object depth z. This inclusion is the key to using the present method to retrieve 3-D images.

2.4 *Retrieval of object information from the cross-spectral density*

To retrieve the object information, we take the product of the cross-spectral density in Eq. (17) and the following function Y_ω, which specifies the in-focus depth z' and the retrieved spectrum $k = \omega/c$:

$$Y_\omega(\Delta\boldsymbol{\rho}_\perp, \hat{\boldsymbol{\rho}}_\perp, z') = \exp\left(-ik \frac{XY}{z'}\right). \quad (18)$$

This function eliminates the quadratic phase factor that appeared in the second expression of Eq. (17) at the in-focus depth. The role of this function is analogues to usual phase transformation function of a thin lens that creates in-focus image of object. The monochromatic component of the retrieved image $O_\omega(x, y, z')$ is expressed as

$$\begin{aligned} O_\omega(x, y, z') = \int &W_\omega(\boldsymbol{R}_0 + \Delta\boldsymbol{\rho}_\perp; \boldsymbol{R}_0 + \hat{\boldsymbol{\rho}}_\perp) Y_\omega(\Delta\boldsymbol{\rho}_\perp, \hat{\boldsymbol{\rho}}_\perp, z') \\ &\times \exp[-i(\boldsymbol{k}'_\perp \cdot \boldsymbol{\rho}'_\perp)] \, d^2\rho'_\perp, \end{aligned} \quad (19)$$

where $k'_x = -kx/z'$, $k'_y = -ky/z'$, and $\boldsymbol{k}'_\perp = (k'_x, k'_y)$. The retrieved image in Eq. (19) is focused on the $z = z'$ plane; objects located at other depths are defocused. This phenomenon is common in ordinary holographic 3-D imaging.

Note that the spectral resolution δk is determined by the reciprocal of the width l_z of the volume interferogram along the Z-axis; thus, $\delta k = 2\pi/l_z$. The transverse resolutions along the x- and y-directions are limited by the corresponding aperture sizes $l_x = l_y = l$ of the alternative complex hologram [the cross-spectral density in Eq. (17)], and the in-focus depth z'. These resolutions, denoted δx and δy, are expressed by $\delta x = \delta y = \lambda F$, where $F = z'/l$ is the effective F-number of the experimental system. We will discuss the longitudinal resolution δz in Sect. 3 in connection with experimental results. The retrieved image sizes along the x (resp. y) direction, denoted $x_{\max}$ (resp. $y_{\max}$), is expressed as $x_{\max} = z'\lambda/\Delta l_x$ (resp. $y_{\max} = z'\lambda/\Delta l_y$), where Δl_x (resp. Δl_y) is the pixel size of the alternative complex hologram along the x (resp. y) direction.

2.5 *The RH volume interferogram*

In this subsection, we discuss the main characteristic of RH volume interferograms. We begin by recalling that an ordinary hologram records the phase distribution of the wavefront propagated from the measured object. In the previously proposed method, which generates S-type volume interferograms, the recorded fringe patterns correspond directly to the phase distributions of the wavefront of many spectral components propagated from the object being measured. Accordingly, the cross-spectral density derived from an S-type volume interferogram corresponds to the ordinary complex hologram. For RH volume interferograms, however, the recorded fringe patterns do not correspond simply to the wavefront propagated from the object. This is because the positions for measuring correlation of the optical field differ between the two methods. The cross-spectral density that is obtained from an S-type volume interferogram is expressed as $W(0, 0, z_0; X, Y, z_0)$; that is, it is the correlation of the monochromatic component of optical fields located at the origin of the observation plane and the point that is sheared two-dimensionally on the observation plane. In contrast, the cross-spectral density obtained from an RH volume interferogram is expressed as $W((X-Y)/2, (Y-X)/2, z_0; (X+Y)/2, (X+Y)/2, z_0)$ [see Eq. (14)]; this means that it represents the correlation of the monochromatic component of the optical field across the observation plane at two points, $\hat{\boldsymbol{\rho}}_\perp$ and $\Delta\boldsymbol{\rho}_\perp$. This difference in cross-spectral density leads to differently shaped fringe patterns in the resultant volume interferograms. Nevertheless, as mentioned in Sect. 2.3, the RH volume interferogram cross-spectral density involves directional and depth information of the object in the linear and quadratic phase factors [see Eq. (17)]. As a consequence, the cross-spectral density decomposed from an RH volume interferogram may be regarded as a kind of complex hologram. Thus, by multiplying a suitable phase function [introduced as Eq. (18)] with the cross-spectral density, the quadratic phase factor is eliminated at the in-focus plane. This enables us to realize 3-D imaging on the basis of RH volume interferograms.

3. Experiment

To verify the method described in Sect. 2, we present

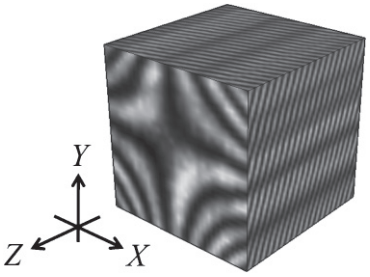

Fig. 3. The experimentally obtained RH volume interferogram for a monochromatic point source located near the origin of the Cartesian coordinate system.

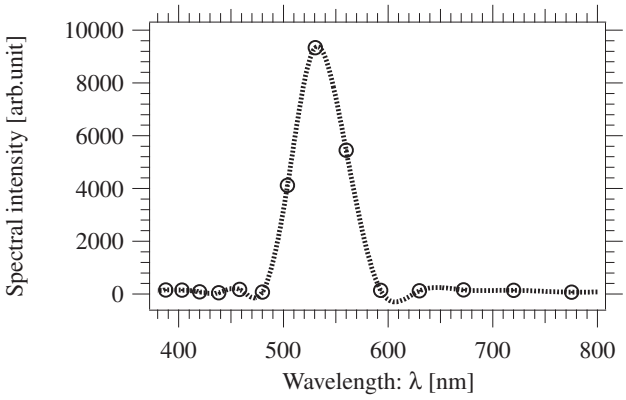

Fig. 4. Spectral profile for the optical field measured over the observation plane.

experimental results for retrieving the spectral components of 3-D images. For the object to be measured, we chose a monochromatic point source, so that the retrieved image corresponded to the impulse response function defined over four-dimensional space (x, y, z, ω). In this experiment, we investigated various imaging characteristics of the present method; depth resolution was of the most interest to us. The monochromatic point source is formed by guiding He–Ne laser light through a single-mode optical fiber, and is set on the x–y stage. The wavelength is 543.5 nm. The distance z between the object and the observation plane is 93 mm. The x–y stage and PZT are moved stepwise at constant intervals. The numbers of steps and intervals are 32 and 12.9 µm for the x–y stage and 64 and 80 nm for PZT, respectively. Then, the 5-D interferogram, measured by this experiment, consists of $32 \times 32 \times 64$ elementally interference patterns. The pixel sizes and numbers of each elementally interference patterns are 12.9 µm square and 32×32, respectively. RH volume interferograms are characterized by the numbers of steps and intervals of the x–y stage and the PZT, x width, y width, and z width. The sizes in our experiment were $l_x = l_y = l = 825.6\,\mu\text{m}$, $\Delta l_x = \Delta l_y = 25.8\,\mu\text{m}$ (in pixel), $l_z = 10.08\,\mu\text{m}$ and $\Delta l_z = 0.16\,\mu\text{m}$ (in pixel). These parameters determine the transverse and longitudinal resolution and the spectral resolution.

The experimental RH volume interferogram was generated by the new selection rule [Eqs. (12a) and (12b)]; it is shown in Fig. 3. The experimentally obtained interferogram has fringe patterns similar to the theoretically predicted patterns, as shown in Fig. 2. By taking the Fourier transform with respect to Z along the center of the volume interferogram, we obtained the spectral profile for the optical field over the observation plane. The result of this is shown in Fig. 4. In this experimental condition, the spectral resolution was $\delta k/2\pi = 992.06\,\text{cm}^{-1}$, which means that $\delta\lambda = 27.97\,\text{nm}$ at $\lambda = 531\,\text{nm}$. The spectral peak was located near 531 nm. Up to spectral resolution, this peak agrees with the peak wavelength of the measured object. Figure 5(a) shows the phase map of the recovered cross-spectral density at the spectral peak of $\lambda = 531\,\text{nm}$. The phase map of the cross-spectral density generated from the same 5-D interferogram data set by the method proposed in Ref. 11 (i.e., an S-type interferogram) is shown in Fig. 5(b) for comparison. The S-type interferogram was precisely the

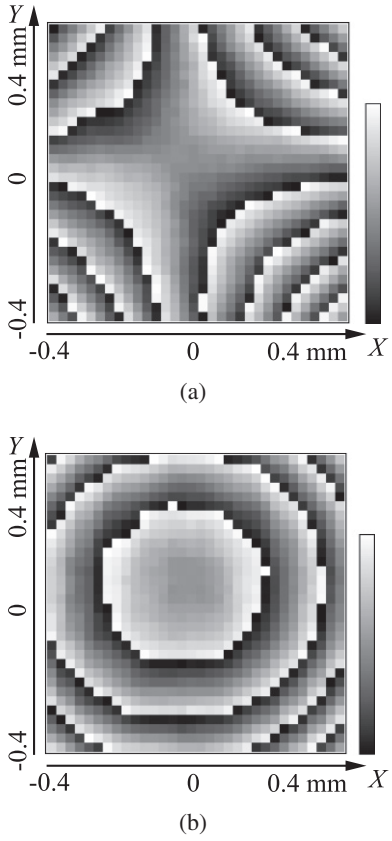

Fig. 5. Phase distributions of the cross-spectral densities at the spectral peak $\lambda = 531\,\text{nm}$ appearing in Fig. 4: (a) present method and (b) S-type method.

phase distribution of the spherical wave propagated from the monochromatic point source. As expected, this was the same phase distribution as obtained by inline phase-shifting holography. However, unlike the S-type interferogram, equal phase surfaces of RH interferograms have a hyperbolic arrangement, in which the phase asymptotes lie along the horizontal and perpendicular lines. This arrangement is also different from the cross-spectral density of H-type interferograms, whose phase asymptotes appear parallel to the lines with direction $\pm 45^\circ$ (see Ref. 13 for details).

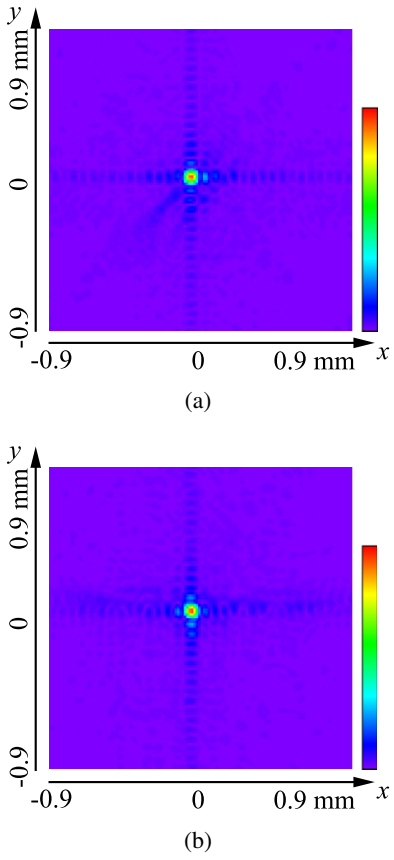

Fig. 6. (Color online) Retrieved in-focus images for monochromatic point source over x–y plane at $z' = 93$ mm: (a) present method and (b) S-type method.

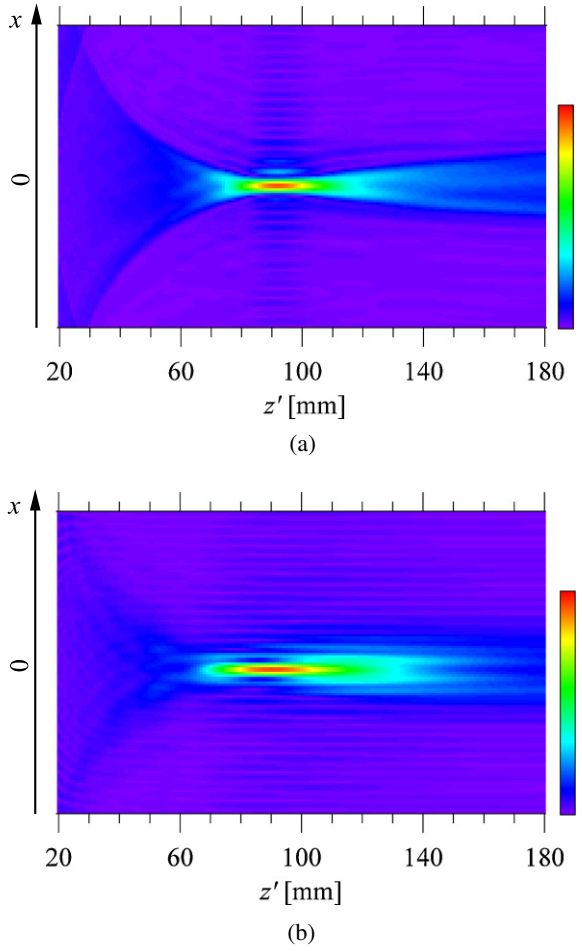

Fig. 7. (Color online) Intensity profile of the monochromatic point source over x–z plane: (a) present method and (b) S-type method.

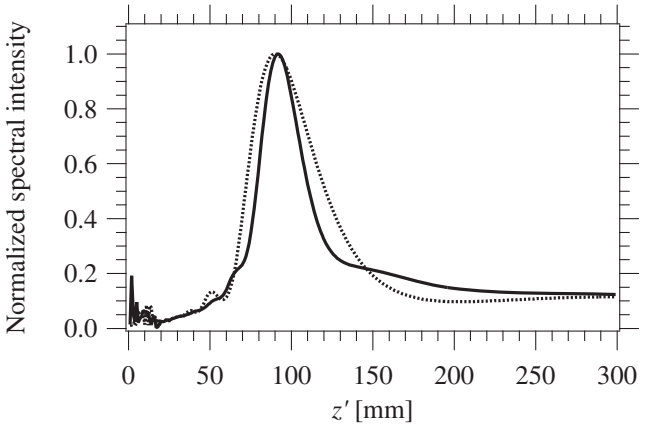

Fig. 8. Comparison of intensity profiles of retrieved images along z-axis: present method (solid line) and S-type method (dotted line).

Figure 6(a) shows the cross sections of the in-focus image (intensity profile) over the x–y plane at $z' = 93$ mm, as retrieved from RH cross-spectral density. In this result, we accounted for the fact that the object information with respect to the x- and y-directions appears with reversed geometry, as suggested in Sect. 2.3. The transverse resolutions were $\delta x = \delta y = 59.81$ µm and the retrieved image sizes were 1.91 mm square. Those transverse imaging properties agree with the values from S-type interferometry, as shown in Fig. 6(b). This agreement arises from the fact that the transverse apertures of the two methods, that is, the measured extensions of the cross-spectral densities, are rectangular of the same size.

The most remarkable difference between the RH and S-type methods appeared in depth resolution. The intensity profiles along the x- and z-axes are shown Figs. 7(a) and 7(b). We found that the intensity peaks were located close to $(x, y, z') = (0\,\text{mm}, 0\,\text{mm}, 93\,\text{mm})$. This difference appears by comparing the intensity profiles; Fig. 8 shows the results of comparison. We found that the RH interferometry showed a narrower intensity peak at the source distance than the S-type interferometry did. The conventional treatment of depth resolution in digital holography is to estimate it by the empirical formula $\delta z = \lambda F^2$. Instead, let us now compare the resolutions quantitatively between the RH method, the S-type method, and the empirical formula estimation.

Table 1 shows a numerical comparison of front half width at half maximum (HWHM), back HWHM, and full width at half maximum (FWHM) for the RH and S-type methods and the empirical formula. We found that the RH method had superior resolution for both front HWHM and back HWHM

Table 1. Numerical comparison of HWHM and FWHM for RH and S-type methods and the empirical formula.

	RH	S-type	λF^2
HWHM (front)/2 (mm)	7	9.5	
HWHM (back)/2 (mm)	10	16	
FWHM/2 (mm)	17	25.5	6.46
Ratio (FWHM/2λF^2)	2.63	3.95	1

than the S-type method did. The depth resolution δz computed as λF^2 was quite small. These results suggest that the depth resolution obtained by the empirical formula is simply an estimate. Finally, we note that the transverse and longitudinal imaging properties of H-type interferometry are the same as those of S-type interferometry (this is shown in Ref. 13). Thus, the present method achieves depth resolution superior to and transverse resolution equivalent to those obtained by the S- and H-type methods. In addition, we have not found any selection rules that give better results than the present one. Therefore, RH volume interferogram will give the best results in depth resolution when compared to results using the other selection rules.

4. Conclusion

We have presented a new coherence three-dimensional imaging spectrometry based on measurement of rotated-hyperbolic volume interferograms. The method uses a new selection rule for reducing a 5-D interferogram to a 3-D volume interferogram. The fringe patterns of the RH volume interferogram do not correspond directly to the wavefront forms of the optical field propagated from the object being measured. Despite this, an RH volume interferogram includes a spatial correlation function with a quadratic phase factor, which means that it contains the 3-D position of the object and continuous spectra for each point on the object. This method thus enables us to retrieve a set of spectral components of 3-D images.

We have presented experimental results for a monochromatic point source. These demonstrated that the 3-D spatial information and spectral information of the measured object were successfully retrieved. Because a spatially incoherent polychromatic object can generally be treated as a sum of uncorrelated point sources, the present method is, in principle, applicable to the retrieval of 3-D spectral images of usual polychromatic objects.

In comparison to the methods proposed in Ref. 11, we find that the present method offered superior depth resolution without degradation in other characteristics. Numerical comparison of the depth resolutions obtained by the RH, S-type, and H-type methods was conducted, and these results were contrasted with the usual estimation formula. From our analysis and experimental results, we conclude that the present method may prove more useful in applications that require high depth resolution, such as optical metrology and biomedical microscopy.

Acknowledgments

This work was supported in part by a Grant-in-Aid for Scientific Research No. 25390087 from the Japan Society for the Promotion of Science.

References

1) A. A. Michelson: Astrophys. J. **51** (1920) 257.
2) K. Itoh, T. Inoue, T. Yoshida, and T. Ichioka: Appl. Opt. **29** (1990) 1625.
3) K. Yoshimori: J. Opt. Soc. Am. A **18** (2001) 765.
4) J. Rosen and A. Yariv: J. Opt. Soc. Am. A **13** (1996) 2091.
5) D. N. Naik, G. Pedrini, and W. Osten: Opt. Express **21** (2013) 3990.
6) M. K. Kim: Opt. Express **21** (2013) 9636.
7) H. Arimoto, K. Yoshimori, and K. Itoh: Opt. Rev. **7** (2000) 25.
8) D. L. Marks, R. A. Stack, and D. J. Brady: Appl. Opt. **38** (1999) 1332.
9) J. Rosen and G. Brooker: Opt. Lett. **32** (2007) 912.
10) D. L. Marks, R. A. Stack, D. J. Brady, D. C. Munson, Jr., and R. B. Brady: Science **284** (1999) 2164.
11) M. Sasamoto and K. Yoshimori: Opt. Rev. **19** (2012) 29.
12) S. Teeranutranont and K. Yoshimori: Appl. Opt. **52** (2013) A388.
13) T. Hashimoto, A. Hirai, and K. Yoshimori: Appl. Opt. **52** (2013) 1497.